A MULTIDIMENSIONAL CODE FOR ISOTHERMAL MAGNETOHYDRODYNAMIC FLOWS IN ASTROPHYSICS

JONGSOO KIM,[1] DONGSU RYU,[2] T. W. JONES,[3] AND SEUNG SOO HONG[4]

ABSTRACT

We present a multidimensional numerical code to solve isothermal magnetohydrodynamic (IMHD) equations for use in modeling astrophysical flows. First we have built a one-dimensional code which is based on an explicit finite-difference method on an Eulerian grid, called the total variation diminishing (TVD) scheme. The TVD scheme is a second-order–accurate extension of the Roe-type upwind scheme. Recipes for building the one-dimensional IMHD code, including the normalized right and left eigenvectors of the IMHD Jacobian matrix, are presented. Then we have extended the one-dimensional code to a multidimensional IMHD code through a Strang-type dimensional splitting. In the multidimensional code, an explicit cleaning step has been included to eliminate nonzero $\nabla \cdot \boldsymbol{B}$ at every time step.

To test the code, IMHD shock tube problems, which encompass all the physical IMHD structures, have been constructed. One-dimensional and two-dimensional shock tube tests have shown that the code captures all the structures correctly without producing noticeable oscillations. Strong shocks are resolved sharply, but weaker shocks spread more. Numerical dissipation (viscosity and resistivity) has been estimated through the decay test of a two-dimensional Alfvén wave. It has been found to be slightly smaller than that of the adiabatic magnetohydrodynamic code based on the same scheme. As an example of astrophysical applications, we have simulated the nonlinear evolution of the two-dimensional Parker instability under a uniform gravity.

Subject headings: instabilities — methods: numerical — MHD — shock waves

1. INTRODUCTION

Over the last two decades, conservative upwind differencing schemes have proven to be very efficient for solving adiabatic hydrodynamic and magnetohydrodynamic (MHD) equations. These methods generally depend on the calculated estimates of mass, momentum, and energy fluxes as well as magnetic field flux across cell boundaries based on the so-called Riemann solutions from the basic conservation laws. Examples for hydrodynamics include extensions of Godunov's scheme (Godunov 1959) such as the MUSCL scheme (Van Leer 1979) and the PPM scheme (Colella & Woodward 1984) as well as those based on approximate flow eigenstates such as the Roe's scheme (Roe 1981), the TVD scheme (Harten 1983), and the ENO scheme (Harten et al. 1987). Works for MHD include Brio & Wu (1988), Zachary & Colella (1992), Zachary, Malagoli, & Colella (1994), Dai & Woodward (1994a, 1994b), Ryu & Jones (1995) (hereafter RJ), Ryu, Jones, & Frank (1995) (hereafter RJF), Powell et al. (1995), and Roe & Balsara (1996). Brio & Wu applied the Roe's approach to the MHD equations. Zachary and collaborators used the BCT scheme to estimate fluxes for the MHD conservation equations. Dai & Woodward adapted the PPM scheme to MHD. Ryu and collaborators extended the Harten's (1983) TVD scheme to MHD. Powell and collaborators developed a Roe-type Riemann solver with an eight-wave structure for MHD. Roe & Balsara constructed one variety of linearized Riemann solutions for MHD. The upwind schemes generally share an ability to sharply and cleanly define fluid discontinuities, especially shocks, and exhibit a robustness that makes them broadly applicable.

The assumption of *adiabatic* flows holds in the limit where cooling is negligible or the cooling timescale is much larger than the dynamical timescale. However, in the other limit, where the cooling timescale is much shorter than the dynamical timescale, the assumption of *isothermal* flows becomes physically more valid (e.g., Draine & McKee 1993 and references therein). Of course, if cooling timescale is comparable to dynamical timescale, cooling should be considered explicitly.

Usually numerical simulations of isothermal flows are made with adiabatic codes by setting the adiabatic index, γ, close to unity. Truelove et al. (1998) showed that with γ as close as to unity as 1.001, their adiabatic hydrodynamic code can follow isothermal collapse without any significant deterioration of accuracy. We also observed that with $\gamma = 1.001$ the adiabatic TVD MHD code (RJ) captures structures in isothermal magnetohydrodynamic (IMHD) shock tubes without noticeable error. Yet, it is desirable to build codes specifically for isothermal flows, since those codes are *simpler* and *faster* than adiabatic ones. That is because the energy conservation equation need not be solved in isothermal codes. As a result, the entropy mode, which carries the contact discontinuity, need not to be considered. In the current paper we describe an IMHD code based on Harten's (1983) TVD scheme. It is the same scheme that was used for the adiabatic MHD code in RJ and RJF. Balsara (1998b) developed an IMHD code also based on an upwind scheme, but his scheme is different from ours.

In § 2 we give recipes for the development of one-dimensional and multidimensional IMHD codes. In § 3, we present the results of tests that include one-dimensional and two-dimensional shock tube problems, the decay of an Alfvén wave, and the nonlinear evolution of the Parker instability under a uniform gravity. Conclusions follow in § 4.

[1] Korea Astronomy Observatory, San 36-1, Hwaam-Dong, Yusong-Ku, Taejon 305-348, Korea and Department of Astronomy, Seoul National University, Seoul 151-742, Korea; jskim@hanul.issa.re.kr.

[2] Department of Astronomy & Space Science, Chungnam National University, Taejon 305-764, Korea; ryu@canopus.chungnam.ac.kr.

[3] Department of Astronomy, University of Minnesota, Minneapolis, MN 55455; twj@msi.umn.edu.

[4] Department of Astronomy, Seoul National University, Seoul 151-742, Korea; sshong@astroism.snu.ac.kr.

2. NUMERICAL SCHEME

2.1. *The Equations for Isothermal Magnetohydrodynamics*

MHDs describes the behavior of the combined system of a conducting fluid and magnetic fields in the limit that the displacement current and the separation between ions and electrons are neglected. So the MHD equations represent coupling of the equations of fluid dynamics with Maxwell's equations of electrodynamics. By ignoring the effects of electrical resistivity, viscosity, and thermal conductivity, and imposing isothermality on the conducting fluid, we get the following IMHD equations:

$$\frac{\partial \rho}{\partial t} + \nabla \cdot (\rho v) = 0 , \tag{2.1}$$

$$\frac{\partial v}{\partial t} + v \cdot \nabla v + \frac{1}{\rho} \nabla(a^2 \rho) - \frac{1}{\rho} (\nabla \times B) \times B = 0 , \tag{2.2}$$

$$\frac{\partial B}{\partial t} - \nabla \times (v \times B) = 0 , \tag{2.3}$$

with an additional constraint,

$$\nabla \cdot B = 0 , \tag{2.4}$$

for the absence of magnetic monopoles. Here a is an isothermal sound speed, and other notations have their usual meanings. We incorporate a factor of $1/(4\pi)^{1/2}$ into the definition of B so that the factor of 4π does not appear in equation (2.2).

In Cartesian coordinates, the above equations are written in a conservative form as

$$\frac{\partial q}{\partial t} + \frac{\partial F_x}{\partial x} + \frac{\partial F_y}{\partial y} + \frac{\partial F_z}{\partial z} = 0 , \tag{2.5}$$

$$q = \begin{pmatrix} \rho \\ \rho v_x \\ \rho v_y \\ \rho v_z \\ B_x \\ B_y \\ B_z \end{pmatrix} , \qquad F_x = \begin{pmatrix} \rho v_x \\ \rho v_x^2 + a^2 \rho + (B_y^2 + B_z^2 - B_x^2)/2 \\ \rho v_x v_y - B_x B_y \\ \rho v_x v_z - B_x B_z \\ 0 \\ v_x B_y - v_y B_x \\ v_x B_z - v_z B_x \end{pmatrix} , \tag{2.6}$$

with F_y and F_z obtained by properly permuting indices. With the state vector q and the flux functions $F_x(q)$, $F_y(q)$, and $F_z(q)$, the Jacobian matrices, $A_x(q) = \partial F_x/\partial q$, $A_y(q) = \partial F_y/\partial q$, and $A_z(q) = \partial F_z/\partial q$ are formed. A system is called *hyperbolic* if all the eigenvalues of the Jacobian matrices are real and distinct and the corresponding set of right eigenvectors is complete (Jeffrey & Taniuti 1964). The system of the ideal, adiabatic MHD equations is known as *nonstrictly hyperbolic*, since some eigenvalues coincide at some points (Brio & Wu 1988; Roe & Balsara 1996). The eigenstructure of the IMHD equations, which is presented in the next subsection, is very similar to that of the adiabatic ones. It is easy to show that the IMHD equations also form a nonstrictly hyperbolic system.

2.2. *One-dimensional Code*

Our strategy for developing a one-dimensional IMHD code is based the TVD scheme (Harten 1983), which was devised to improve the first-order–accurate Roe's upwind scheme (Roe 1981) into a second-order–accurate one. We derive for it the eigenvalues and eigenvectors of the system of the IMHD equations, which are given below. With the eigenvalues and eigenvectors, it is straightforward to apply the construction procedure for the one-dimensional adiabatic MHD code (RJ) to an isothermal analogue. Even though the procedure is described in RJ, we here repeat it to make this paper self-contained. Special attention is given to the orthonormal eigenvectors of the system of the IMHD equations.

We consider, as an example, plane-symmetric, one-dimensional flows exhibiting variation along the x-direction. Then y- and z-derivatives in equation (2.5) are zero, and we have the one-dimensional IMHD equations

$$\frac{\partial q}{\partial t} + \frac{\partial F_x}{\partial x} = 0 , \tag{2.7}$$

where q and F_x are defined in equation (2.6). The fifth equation in the system of equation (2.7) is $\partial B_x/\partial t = 0$, and the constraint in equation (2.4) is $\partial B_x/\partial x = 0$. These imply that initially B_x should be spatially constant and should be kept constant during the evolution of the flow. So we need not include the equation for B_x in a one-dimensional code.

The Jacobian matrix $\partial F_x/\partial q$ of the system of equation (2.7) is given by

$$A_x = \begin{pmatrix} 0 & 1 & 0 & 0 & 0 & 0 \\ a^2 - v_x^2 & 2v_x & 0 & 0 & b_y\sqrt{\rho} & b_z\sqrt{\rho} \\ -v_x v_y & v_y & v_x & 0 & -b_x\sqrt{\rho} & 0 \\ -v_x v_z & v_z & 0 & v_x & 0 & -b_x\sqrt{\rho} \\ -v_x\dfrac{b_y}{\sqrt{\rho}} + v_y\dfrac{b_x}{\sqrt{\rho}} & \dfrac{b_y}{\sqrt{\rho}} & -\dfrac{b_x}{\sqrt{\rho}} & 0 & v_x & 0 \\ -v_x\dfrac{b_z}{\sqrt{\rho}} + v_z\dfrac{b_x}{\sqrt{\rho}} & \dfrac{b_z}{\sqrt{\rho}} & \dfrac{b_z}{\sqrt{\rho}} & 0 & -\dfrac{b_x}{\sqrt{\rho}} & 0 & v_x \end{pmatrix}, \tag{2.8}$$

where $b_{x,y,z} = B_{x,y,z}/\sqrt{\rho}$. The six eigenvalues in nondecreasing order are

$$a_1 = v_x - c_f, \qquad a_2 = v_x - c_a, \qquad a_3 = v_x - c_s,$$
$$a_4 = v_x + c_s, \qquad a_5 = v_x + c_a, \qquad a_6 = v_x + c_f, \tag{2.9}$$

where c_f, c_a, c_s are the fast, Alfvén, and slow characteristic speeds, respectively. There is no entropy mode for the IMHD equations. The quantities $a_1, \ldots, a_6$ represent the six speeds with which information is propagated locally by three MHD wave families. The three characteristic speeds are expressed as

$$c_f = \{\tfrac{1}{2}\,[a^2 + b_x^2 + b_y^2 + b_z^2 + \sqrt{(a^2 + b_x^2 + b_y^2 + b_z^2)^2 - 4a^2 b_x^2}]\}^{1/2},$$
$$c_a = |b_x|,$$
$$c_s = \{\tfrac{1}{2}\,[a^2 + b_x^2 + b_y^2 + b_z^2 - \sqrt{(a^2 + b_x^2 + b_y^2 + b_z^2)^2 - 4a^2 b_x^2}]\}^{1/2}. \tag{2.10}$$

The six right eigenvectors corresponding to the six eigenvalues are

$$R_{v_x \pm c_f} = \begin{pmatrix} 1 \\ v_x \pm c_f \\ v_y \mp \dfrac{c_f b_x b_y}{c_f^2 - b_x^2} \\ v_z \mp \dfrac{c_f b_x b_z}{c_f^2 - b_x^2} \\ \dfrac{c_f^2 b_y}{(c_f^2 - b_x^2)\sqrt{\rho}} \\ \dfrac{c_f^2 b_z}{(c_f^2 - b_x^2)\sqrt{\rho}} \end{pmatrix}, \quad R_{v_x \pm c_a} = \begin{pmatrix} 0 \\ 0 \\ \mp b_z\,\mathrm{sgn}\,(b_x) \\ \pm b_y\,\mathrm{sgn}\,(b_x) \\ \dfrac{b_z}{\sqrt{\rho}} \\ -\dfrac{b_y}{\sqrt{\rho}} \end{pmatrix}, \quad R_{v_x \pm c_s} = \begin{pmatrix} 1 \\ v_x \pm c_s \\ v_y \mp \dfrac{c_s b_x b_y}{c_s^2 - b_x^2} \\ v_z \mp \dfrac{c_s b_x b_z}{c_s^2 - b_x^2} \\ \dfrac{c_s^2 b_y}{(c_s^2 - b_x^2)\sqrt{\rho}} \\ \dfrac{c_s^2 b_z}{(c_s^2 - b_x^2)\sqrt{\rho}} \end{pmatrix}. \tag{2.11}$$

Near the point where either $b_x = 0$ or $b_y = b_z = 0$, the above right eigenvectors are not well defined, with some elements becoming singular. By renormalizing the eigenvectors, the singularities can be removed. The renormalized right eigenvectors are

$$R_{v_x \pm c_f} = \begin{pmatrix} \alpha_f \\ \alpha_f(v_x \pm c_f) \\ \alpha_f v_y \mp \alpha_s \beta_y b_x \\ \alpha_f v_z \mp \alpha_s \beta_z b_x \\ \dfrac{\alpha_s \beta_y c_f}{\sqrt{\rho}} \\ \dfrac{\alpha_s \beta_z c_f}{\sqrt{\rho}} \end{pmatrix}, \quad R_{v_x \pm c_a} = \begin{pmatrix} 0 \\ 0 \\ \mp \beta_z\,\mathrm{sgn}\,(b_x) \\ \pm \beta_y\,\mathrm{sgn}\,(b_x) \\ \dfrac{\beta_z}{\sqrt{\rho}} \\ -\dfrac{\beta_y}{\sqrt{\rho}} \end{pmatrix}, \quad R_{v_x \pm c_s} = \begin{pmatrix} \alpha_s \\ \alpha_s(v_x \pm c_s) \\ \alpha_s v_y \pm \alpha_f \beta_y a\,\mathrm{sgn}\,(b_x) \\ \alpha_s v_z \pm \alpha_f \beta_z a\,\mathrm{sgn}\,(b_x) \\ -\dfrac{\alpha_f \beta_y a^2}{c_f \sqrt{\rho}} \\ -\dfrac{\alpha_f \beta_z a^2}{c_f \sqrt{\rho}} \end{pmatrix}, \tag{2.12}$$

where α's and β's are defined by

$$\alpha_f = \frac{\sqrt{c_f^2 - b_x^2}}{\sqrt{c_f^2 - c_s^2}}, \qquad \alpha_s = \frac{\sqrt{c_f^2 - a^2}}{\sqrt{c_f^2 - c_s^2}}, \qquad \beta_y = \frac{b_y}{\sqrt{b_y^2 + b_z^2}}, \qquad \beta_z = \frac{b_z}{\sqrt{b_y^2 + b_z^2}}. \tag{2.13}$$

At the points where $b_y = b_z = 0$, β's are defined as a limiting value, i.e.,

$$\beta_y = \beta_z = \frac{1}{\sqrt{2}}. \tag{2.14}$$

Similarly, at the point where $b_y = b_z = 0$ and $b_x^2 = a^2$, α's are defined as

$$\alpha_f = \alpha_s = 1 . \tag{2.15}$$

The left eigenvectors, which are orthonormal to the right eigenvectors, $L_l \cdot R_m = \delta_{lm}$, are

$$L_{v_x \pm c_f} = (l^{(1)}_{v_x \pm c_f}, l^{(2)}_{v_x \pm c_f}, l^{(3)}_{v_x \pm c_f}, l^{(4)}_{v_x \pm c_f}, l^{(5)}_{v_x \pm c_f}, l^{(6)}_{v_x \pm c_f}) , \tag{2.16}$$

with

$$l^{(1)}_{v_x \pm c_f} = \frac{1}{\theta_1} \alpha_f a^2 \pm \frac{1}{\theta_2} [-\alpha_f a v_x + \alpha_s c_s (\beta_y v_y + \beta_z v_z) \operatorname{sgn}(b_x)] , \qquad l^{(2)}_{v_x \pm c_f} = \pm \frac{1}{\theta_2} \alpha_f a ,$$

$$l^{(3)}_{v_x \pm c_f} = \mp \frac{1}{\theta_2} \alpha_s \beta_y c_s \operatorname{sgn}(b_x) , \qquad l^{(4)}_{v_x \pm c_f} = \mp \frac{1}{\theta_2} \alpha_s \beta_z c_s \operatorname{sgn}(b_x) ,$$

$$l^{(5)}_{v_x \pm c_f} = \frac{1}{\theta_1} \alpha_s \beta_y c_f \sqrt{\rho} , \qquad l^{(6)}_{v_x \pm c_f} = \frac{1}{\theta_1} \alpha_s \beta_z c_f \sqrt{\rho} ,$$

$$L_{v_x \pm c_a} = (l^{(1)}_{v_x \pm c_a}, l^{(2)}_{v_x \pm c_a}, l^{(3)}_{v_x \pm c_a}, l^{(4)}_{v_x \pm c_a}, l^{(5)}_{v_x \pm c_a}, l^{(6)}_{v_x \pm c_a}) , \tag{2.17}$$

with

$$l^{(1)}_{v_x \pm c_a} = \pm \tfrac{1}{2} (\beta_z v_y - \beta_y v_z) \operatorname{sgn}(b_x) , \qquad l^{(2)}_{v_x \pm c_a} = 0 , \qquad l^{(3)}_{v_x \pm c_a} = \mp \tfrac{1}{2} \beta_z \operatorname{sgn}(b_x) ,$$

$$l^{(4)}_{v_x \pm c_a} = \pm \tfrac{1}{2} \beta_y \operatorname{sgn}(b_x) , \qquad l^{(5)}_{v_x \pm c_a} = \tfrac{1}{2} \beta_z \sqrt{\rho}, \qquad l^{(6)}_{v_x \pm c_a} = -\tfrac{1}{2} \beta_y \sqrt{\rho} ,$$

and

$$L_{v_x \pm c_s} = (l^{(1)}_{v_x \pm c_s}, l^{(2)}_{v_x \pm c_s}, l^{(3)}_{v_x \pm c_s}, l^{(4)}_{v_x \pm c_s}, l^{(5)}_{v_x \pm c_s}, l^{(6)}_{v_x \pm c_s}) , \tag{2.18}$$

with

$$l^{(1)}_{v_x \pm c_s} = \frac{1}{\theta_1} \alpha_s c_f^2 \mp \frac{1}{\theta_2} [\alpha_s c_a v_x + \alpha_f c_f (\beta_y v_y + \beta_z v_z) \operatorname{sgn}(b_x)] , \qquad l^{(2)}_{v_x \pm c_s} = \pm \frac{1}{\theta_2} \alpha_s c_a ,$$

$$l^{(3)}_{v_x \pm c_s} = \pm \frac{1}{\theta_2} \alpha_f \beta_y c_f \operatorname{sgn}(b_x) , \qquad l^{(4)}_{v_x \pm c_s} = \pm \frac{1}{\theta_2} \alpha_f \beta_z c_f \operatorname{sgn}(b_x) ,$$

$$l^{(5)}_{v_x \pm c_s} = -\frac{1}{\theta_1} \alpha_f \beta_y c_f \sqrt{\rho} , \qquad l^{(6)}_{v_x \pm c_s} = -\frac{1}{\theta_1} \alpha_f \beta_z c_f \sqrt{\rho} ,$$

where

$$\theta_1 = 2(\alpha_f^2 a^2 + \alpha_s^2 c_f^2) , \qquad \theta_2 = 2(\alpha_f^2 c_f a + \alpha_s^2 c_a c_s) . \tag{2.19}$$

Some elements in the normalized right and left eigenvectors are not continuous. In order to force them to be continuous,

$$\operatorname{sgn}(b_T) = \begin{cases} 1 , & \text{if } b_y > 0 \text{ or } b_y = 0, \text{ and } b_z > 0 ; \\ -1 , & \text{if } b_y < 0 \text{ or } b_y = 0, \text{ and } b_z < 0 , \end{cases} \tag{2.20}$$

is multiplied to $R_{v_x \pm c_s}$ and $L_{v_x \pm c_s}$ if $a^2 > c_a^2$, and to $R_{v_x \pm c_f}$ and $L_{v_x \pm c_f}$ if $a^2 < c_a^2$.

Note that our eigenvectors have a different form from those derived in Balsara (1998a). The exact form of the eigenvectors does not matter once all the singular points are taken care of.

Here we use the conventional indices. The superscript n represents the time step. The subscript i indicates quantities at the cell center, while $i + \frac{1}{2}$ marks those at the right-hand cell boundary. The subscript k represents the characteristic fields, with the order that $k = 1$ is for the field associated with eigenvalue $v_x - c_f$, $k = 2$ is for the field with $v_x - c_a$, $k = 3$ is for the field with $v_x - c_s$, $k = 4$ for the field with $v_x + c_s$, $k = 5$ for the field with $v_x + c_a$, and finally $k = 6$ for the field with $v_x + c_f$.

An important step in the Roe (1981) scheme is to determine a Roe matrix $\bar{A}_{x,i+1/2}(q_i, q_{i+1})$ at the cell boundary from the adjacent state vectors, which satisfies the Roe's suggested properties. One of them is $F_{x,i+1} - F_{x,i} = \bar{A}_{x,i+1/2}(q_{i+1} - q_i)$. For the systems of the adiabatic and isothermal hydrodynamic equations, there exists a Roe matrix evaluated at the $\sqrt{\rho}$-weighted average state (Roe 1981; LeVeque 1997). For the system of the adiabatic MHD equations, there is, however, no simple form of the Roe matrix except for the case with an adiabatic index $\gamma = 2$ (Brio & Wu 1988). We also have failed to find a simple form of the Roe matrix for the system of the IMHD equations. So we use an arithmetic averaging for the flow quantities at the cell boundary in the IMHD code, which was shown to work well in the adiabatic MHD code (RJ):

$$\rho_{i+1/2} = \frac{\rho_i + \rho_{i+1}}{2} , \tag{2.21}$$

$$v_{x,i+1/2} = \frac{v_{x,i} + v_{x,i+1}}{2} , \qquad v_{y,i+1/2} = \frac{v_{y,i} + v_{y,i+1}}{2} , \qquad v_{z,i+1/2} = \frac{v_{z,i} + v_{z,i+1}}{2} , \tag{2.22}$$

$$B_{y,i+1/2} = \frac{B_{y,i} + B_{y,i+1}}{2} , \qquad B_{z,i+1/2} = \frac{B_{z,i} + B_{z,i+1}}{2} . \tag{2.23}$$

The state vector q at the cell center is updated by calculating the modified fluxes $\bar{f}_x$ at the cell boundaries as follows:

$$L_x q_i^{n+1} = q_i^n - \frac{\Delta t^n}{\Delta x} (\bar{f}_{x,i-1/2} - \bar{f}_{x,i+1/2}) , \tag{2.24}$$

$$\bar{f}_{x,i+1/2} = \frac{1}{2} [F_x(q_i^n) + F_x(q_{i+1}^n)] - \frac{\Delta x}{2\Delta t^n} \sum_{k=1}^{6} \beta_{k,i+1/2} R_{k,i+1/2}^n , \tag{2.25}$$

$$\beta_{k,i+1/2} = Q_k\left(\frac{\Delta t^n}{\Delta x} a_{k,i+1/2}^n + \gamma_{k,i+1/2}\right)\alpha_{k,i+1/2} - (g_{k,i} + g_{k,i+1}) , \tag{2.26}$$

$$\alpha_{k,i+1/2} = L_{k,i+1/2}^n(q_{i+1}^n - q_i^n) , \tag{2.27}$$

$$\gamma_{k,i+1/2} = \begin{cases} \dfrac{g_{k,i+1} - g_{k,i}}{\alpha_{k,i+1/2}} & \text{for } \alpha_{k,i+1/2} \neq 0 , \\ 0 & \text{for } \alpha_{k,i+1/2} = 0 , \end{cases} \tag{2.28}$$

$$g_{k,i} = \text{sgn} (\tilde{g}_{k,i+1/2}) \max \{0, \min [|\tilde{g}_{k,i+1/2}|, \tilde{g}_{k,i-1/2} \, \text{sgn} (\tilde{g}_{k,i+1/2})]\} ; \tag{2.29}$$

$$\tilde{g}_{k,i+1/2} = \frac{1}{2} \left[Q_k\left(\frac{\Delta t^n}{\Delta x} a_{k,i+1/2}^n\right) - \left(\frac{\Delta t^n}{\Delta x} a_{k,i+1/2}^n\right)^2 \right]\alpha_{k,i+1/2} , \tag{2.30}$$

$$Q_k(\chi) = \begin{cases} \dfrac{\chi^2}{4\epsilon_k} + \epsilon_k & \text{for } |\chi| < 2\epsilon_k , \\ |\chi| & \text{for } |\chi| \geq 2\epsilon_k . \end{cases} \tag{2.31}$$

Since the use of *contact steepener* and *rotational steepener* produces spurious numerical oscillations in the adiabatic MHD code (RJ; RJF), we do not include the rotational steepener in the IMHD code. The time step size Δt^n is restricted by the usual Courant condition for stability, $\Delta t^n = C_{\text{cour}} \Delta x / \max (|v_{x,i+1/2}^n| + c_{f,i+1/2}^n)$, with $C_{\text{cour}} < 1$.

2.3. Multidimensional Code

We extend the one-dimensional IMHD code to more dimensions by using a Strang-type directional splitting (Strang 1968). Here we explain, as an example, the implementation of it in two-dimensional plane-parallel geometry. The two-dimensional IMHD equations written in the conservative form (eq. [2.5]) can be split into

$$L_x(x\text{-sweep}): q_t + \frac{\partial F_x}{\partial x} = 0 ; \qquad L_y(y\text{-sweep}): q_t + \frac{\partial F_y}{\partial y} = 0 . \tag{2.32}$$

In a time step, we update the state vector $q(x, y)$ along the x-direction with y fixed, followed along the y-direction with x fixed,

$$q^{n+1} = L_y L_x q^n . \tag{2.33}$$

In order to maintain a second-order accuracy in time, the order of directional sweeps is permuted in the next time step by $L_x L_y$. The time step size, Δt, is calculated at the start of the one complete sequence of $L_x L_y \, L_y L_x$ and fixed through the sequence.

In multidimensional simulations, numerical solutions may not satisfy $\nabla \cdot B = 0$ because of discretization errors. Brackbill & Barnes (1980) pointed out that errors of nonzero $\nabla \cdot B$ appear as a force parallel to the field. Nonzero $\nabla \cdot B$ can be removed, for instances, either by incorporating an explicit *divergence cleaning* method as described in RJF or by implementing a scheme similar to the *constrained transport* scheme (Evans & Hawley 1988), which was described in detail for the adiabatic MHD code in Ryu et al. (1998). Tests in the next section have been done using the explicit divergence cleaning method, and the next two paragraphs describe it briefly.

At the beginning of MHD simulations, $\nabla \cdot B = 0$ is satisfied. The updated magnetic field B, which is not in general divergence-free, can be decomposed as into two parts,

$$B = -\nabla\phi + \nabla \times V , \tag{2.34}$$

where ϕ and V are scalar and vector functions, respectively. Then the corrected magnetic field defined as $B^c = B + \nabla\phi$ becomes divergence-free. So the problem of the divergence-cleaning is reduced to find ϕ, which is described by the Poisson equation

$$\nabla^2\phi = -\nabla \cdot B . \tag{2.35}$$

In two-dimensional Cartesian geometry, for instance, the following finite difference representations

$$B^c_{x,i,j} = B_{x,i,j} + \frac{\phi_{i+1,j} - \phi_{i-1,j}}{2\Delta x} \,, \qquad B^c_{y,i,j} = B_{y,i,j} + \frac{\phi_{i,j+1} - \phi_{i,j-1}}{2\Delta y} \,, \tag{2.36}$$

together with

$$\frac{\phi_{i+2,j} - 2\phi_{i,j} + \phi_{i-2,j}}{(2\Delta x)^2} + \frac{\phi_{i,j+2} - 2\phi_{i,j} + \phi_{i,j-2}}{(2\Delta y)^2} = -\left(\frac{B_{x,i+1,j} - B_{x,i-1,j}}{2\Delta x} + \frac{B_{y,i,j+1} - B_{y,i,j-1}}{2\Delta y}\right), \tag{2.37}$$

ensures

$$\frac{B^c_{x,i+1,j} - B^c_{x,i-1,j}}{2\Delta x} + \frac{B^c_{y,i,j+1} - B^c_{x,i,j-1}}{2\Delta y} = 0 \,, \tag{2.38}$$

within machine round-off error. Extensions to the three-dimension and/or to other geometry are straightforward.

Equation (2.37) is solved with boundary conditions specific to problems. In the problems with periodic boundaries (as in the decay test of the Alfvén wave in § 3.2), a fast Poisson solver based on the fast Fourier transform can be used. In the nonlinear simulation of the Parker instability in § 3.3 with reflection boundaries along one direction, the computational domain is doubled to that direction and the resulting boundaries are enforced to be periodic. In the two-dimensional shock tube tests in § 3.1.2, doubling the computational domain in both directions also makes the resulting boundaries periodic. Note that in equation (2.37) ϕ's are coupled with those at every other cell in a column and row. So the (extended) computational domain is divided into four subdomains, and ϕ's are computed in those subdomains separately.

3. TESTS

In this section we present the results of three tests. The first and the second are isothermal versions of MHD shock tubes and decay of an Alfvén wave, respectively (RJ; RJF). The shock tube test shows the ability of the IMHD code to handle all the three MHD wave family structures, while the decay test of an Alfvén wave measures numerical dissipation. The third test is the simulation of a real astrophysical situation, the nonlinear evolution of the Parker instability under a uniform gravity. In all the tests, we set the isothermal speed $a = 1$.

3.1. Shock Tube Tests

Based on the work of RJ, we have devised four shock tube problems that include discontinuities and rarefaction waves of IMHDs. To confirm the validity of our numerical solutions we have compared them to the analytic solutions obtained with an exact, nonlinear MHD Riemann solver described in RJ. That Riemann solver iterates from an initial guess of the solution for the full set of MHD waves based on the given left and right states. Iteration continues until the solutions to the innermost wave zone reached from the two opposite directions agree within some specified limit (in practice, a relative error 10^{-5}). The four shock tube solutions that we have applied in the test described below are listed in Table 1. $C_{\mathrm{cour}} = 0.8$ and $\epsilon_1 = \epsilon_6 = 0.3$ (for fast modes), $\epsilon_2 = \epsilon_5 = 0.0$ (for Alfvén modes), $\epsilon_3 = \epsilon_4 = 0.3$ (for slow modes) have been used in the shock tube test calculations.

3.1.1. One-dimensional Shock Tube Tests

The one-dimensional simulations of the shock tube problems have been done with 512 cells in a computational tube bounded by $x = [0,1]$. We plot in the following figures the resulting ρ, B_y, B_z, v_x, v_y, and v_z at each cell with open circles and the analytic solutions with lines.

Figure 1a shows the result of the first shock tube problem at $t = 0.1$ with the initial condition of a left state $[\rho = 1, v_x = 0, v_y = 0, v_z = 0, B_y = 5/(4\pi)^{1/2}, B_z = 0]$, a right state $[\rho = 0.1, v_x = 0, v_y = 0, v_z = 0, B_y = 2/(4\pi)^{1/2}, B_z = 0]$, and $B_x = 3/(4\pi)^{1/2}$. It exhibits the capturing of a fast rarefaction wave, a slow rarefaction wave, a slow shock, and a fast shock whose structures are plotted in the figure from left to right. There is no contact discontinuity. The fast and slow shocks are resolved sharply within several cells. In order to see the capturing rotational discontinuities, we have set up the initial condition of the second shock tube problem as a left state $[\rho = 1.08, v_x = 1.2, v_y = 0.01, v_z = 0.5, B_y = 3.6/(4\pi)^{1/2}, B_z = 2/(4\pi)^{1/2}]$, a right state $[\rho = 1, v_x = 0, v_y = 0, v_z = 0, B_y = 4/(4\pi)^{1/2}, B_z = 2/(4\pi)^{1/2}]$, and $B_x = 2/(4\pi)^{1/2}$. Figure 1b shows the result at $t = 0.2$. There are two fast shocks propagating outmost, and two slow shocks interior to those. Two rotational discontinuities lie between the fast and slow shocks. Here the strong fast shocks are resolved sharply, but the weak slow shocks and rotational discontinuities spread over more cells. The third shock tube problem has been set up with the initial condition of a left state $[\rho = 0.12, \quad v_x = 24, v_y = 0, v_z = 0, B_y = 3/(4\pi)^{1/2}, B_z = 0]$, a right state $[\rho = 0.3, v_x = -15, v_y = 0, v_z = 0, B_y = 0, B_z = 3/(4\pi)^{1/2}]$, and $B_x = 0$. Two oppositely moving magnetosonic shocks and a tangential discontinuity at $t = 0.2$ are shown in Figure 1c. The magnetosonic shocks are again resolved sharply, but the tangential discontinuity spreads over ~ 20 cells. In the fourth shock tube problem, the initial condition has been set up with a left state $(\rho = 1, v_x = -1, v_y = 0, v_z = 0, B_y = 1, B_z = 0)$, a right state $(\rho = 1, v_x = 1, v_y = 0, v_z = 0, B_y = 1, B_z = 0)$, and $B_x = 0$. The result at $t = 0.16$ in Figure 1d shows two oppositely moving identical magnetosonic rarefactions.

3.1.2. Two-dimensional Shock Tube Tests

The two-dimensional simulations of the shock tube problems have been done with 256×256 cells in a computational domain bounded by $x = [0,1]$ and $y = [0,1]$. Initially, the domain is divided into two parts by a diagonal line joining the two points $(0, 1)$ and $(1, 0)$. The left state of the initial conditions for the one-dimensional shock tube problems has been assigned to

TABLE 1

SHOCK TUBE TEST

ρ	v_x	v_y	v_z	B_y	B_z
Test 1: $B_x = 8.4628\text{E}-01$					
1.0000E+00......	0.0000E+00	0.0000E+00	0.0000E+00	1.4105E+00	0.0000E+00
5.7648E−01......	9.3200E−01	−5.3737E−01	0.0000E+00	5.9825E−01	0.0000E+00
3.0968E−01......	1.3718E+00	−1.0767E−02	0.0000E+00	7.8902E−01	0.0000E+00
1.2358E−01......	7.2565E−01	−7.6338E−01	0.0000E+00	9.0720E−01	0.0000E+00
1.0000E−01......	0.0000E+00	0.0000E+00	0.0000E+00	5.6419E−01	0.0000E+00
Test 2: $B_x = 5.6419\text{E}-01$					
1.0800E+00......	1.2000E+00	1.0000E−02	5.0000E−01	1.0155E+00	5.6419E−01
1.5087E+00......	6.4673E−01	1.3132E−01	5.6740E−01	1.4677E+00	8.1542E−01
1.5087E+00......	6.4673E−01	2.4196E−01	3.0857E−01	1.6036E+00	4.9750E−01
1.7451E+00......	6.0765E−01	7.3388E−02	2.5628E−01	1.4736E+00	4.5716E−01
1.3560E+00......	5.4030E−01	−2.1440E−01	1.6699E−01	1.6825E+00	5.2198E−01
1.3560E+00......	5.4030E−01	−1.2262E−01	−6.1311E−02	1.5757E+00	7.8783E−01
1.0000E+00......	0.0000E+00	0.0000E+00	0.0000E+00	1.1284E+00	5.6419E−01
Test 3: $B_x = 0.0000\text{E}+00$					
1.2000E−01......	2.4000E+01	2.3130E−16	0.0000E+00	8.4628E−01	4.4409E−16
1.7079E+00......	9.2149E−02	2.3130E−16	0.0000E+00	1.2045E+01	6.3206E−15
4.1960E+00......	9.2149E−02	0.0000E+00	0.0000E+00	7.2478E−16	1.1837E+01
3.0000E−01......	−1.5000E+01	0.0000E+00	0.0000E+00	0.0000E+00	8.4628E−01
Test 4: $B_x = 0.0000\text{E}+00$					
1.0000E+00......	−1.0000E+00	0.0000E+00	0.0000E+00	1.0000E+00	0.0000E+00
4.6392E−01......	7.8159E−08	0.0000E+00	0.0000E+00	4.6392E−01	0.0000E+00
1.0000E+00......	1.0000E+00	0.0000E+00	0.0000E+00	1.0000E+00	0.0000E+00

the lower left part and the right state to the upper right part. The generated structures, including discontinuities and rarefactions, propagate parallel to the other diagonal line joining the two points (0, 0) and (1, 1).

In Figures 2a and 2b, two-dimensional correspondences of Figures 1a and 1b are plotted. In the figures, the following subscripts are used: ‖ for parallel components of velocity and magnetic field along the diagonal line joining the two points (0, 0) and (1, 1), ⊥ for perpendicular components that are still in the computational plane, and z for components that are out of the plane. Although the resolution of the two-dimensional simulations, 256 × 256 cells, is lower than that of the one-dimensional ones, 512 cells, we see that all the structures have been captured correctly.

3.2. Decay of an Alfvén Wave

RJF carried out a test of the decay of linear waves in order to estimate numerical dissipations (resistivity and viscosity) in their adiabatic MHD code. Following the same idea, the decay of a linear Alfvén wave has been calculated and numerical dissipation in our IMHD code has been estimated. The IMHD equations for viscous and resistive fluid can be written as

$$\frac{\partial \rho}{\partial t} + \nabla \cdot (\rho v) = 0 \; , \tag{3.1}$$

$$\frac{\partial v}{\partial t} + v \cdot \nabla v + \frac{1}{\rho} \nabla(a^2 \rho) - \frac{1}{\rho} (\nabla \times B) \times B = \frac{1}{\rho} \partial_k \sigma_{ik} \; , \tag{3.2}$$

$$\frac{\partial B}{\partial t} - \nabla \times (v \times B) = \eta \nabla^2 B \; . \tag{3.3}$$

In the momentum equation, the viscosity tensor σ_{ik} is given by

$$\sigma_{ik} = \mu(\partial_k v_i + \partial_i v_k - \tfrac{2}{3}\delta_{ik} \nabla \cdot v) + \zeta \delta_{ik} \nabla \cdot v \; , \tag{3.4}$$

where μ and ζ are the dynamic shear and bulk viscosity, and η is the electrical resistivity. Under uniform density, ρ_0, and uniform magnetic field, $B = B_0 \hat{x}$, the complex angular frequency of Alfvén waves is predicted from the linear analysis to be

$$\omega = \frac{i}{2}\left(\frac{\mu}{\rho_0} + \eta\right)k^2 \pm c_A k\left[1 - \frac{1}{4c_A^2}\left(\frac{\mu}{\rho_0} - \eta\right)^2 k^2\right]^{1/2} \; , \tag{3.5}$$

where $c_A = (B_0^2/2\rho_0)^{1/2}$ is the Alfvén speed along the wave propagation direction and $k = (k_x^2 + k_y^2)^{1/2}$ is the total wavenumber. Note that the complex angular frequency of the isothermal Alfvén waves is exactly the same as that of the adiabatic ones
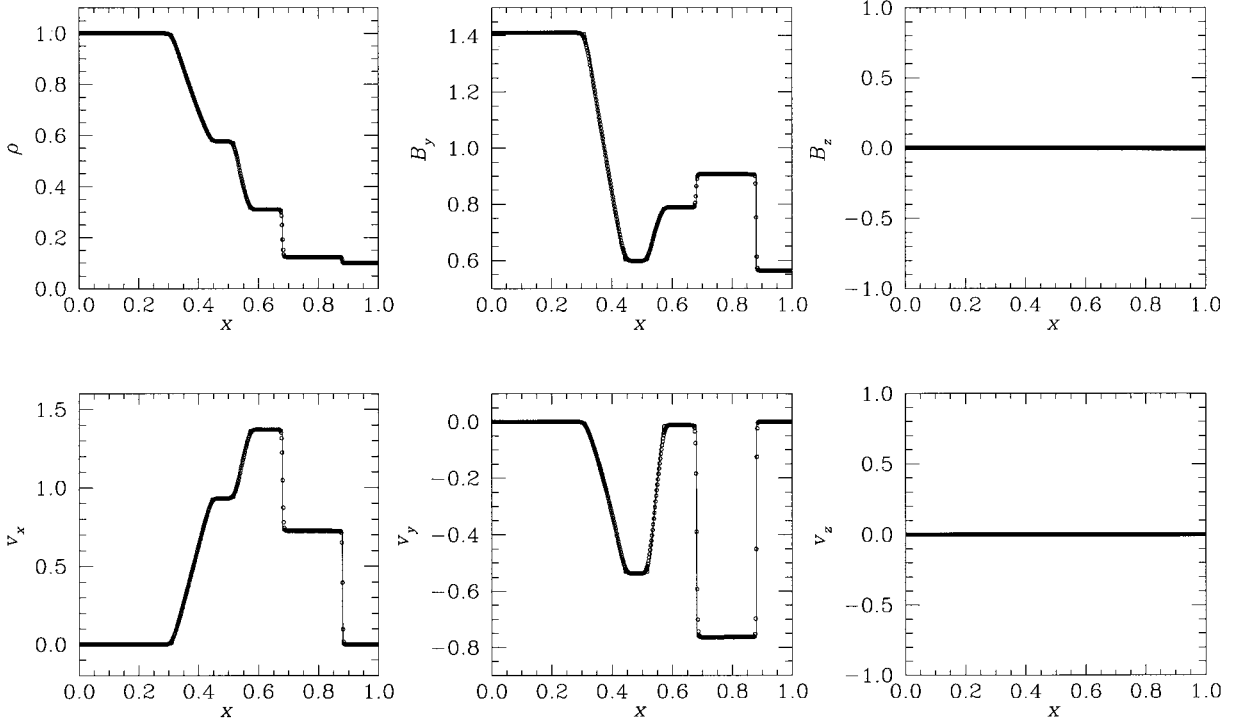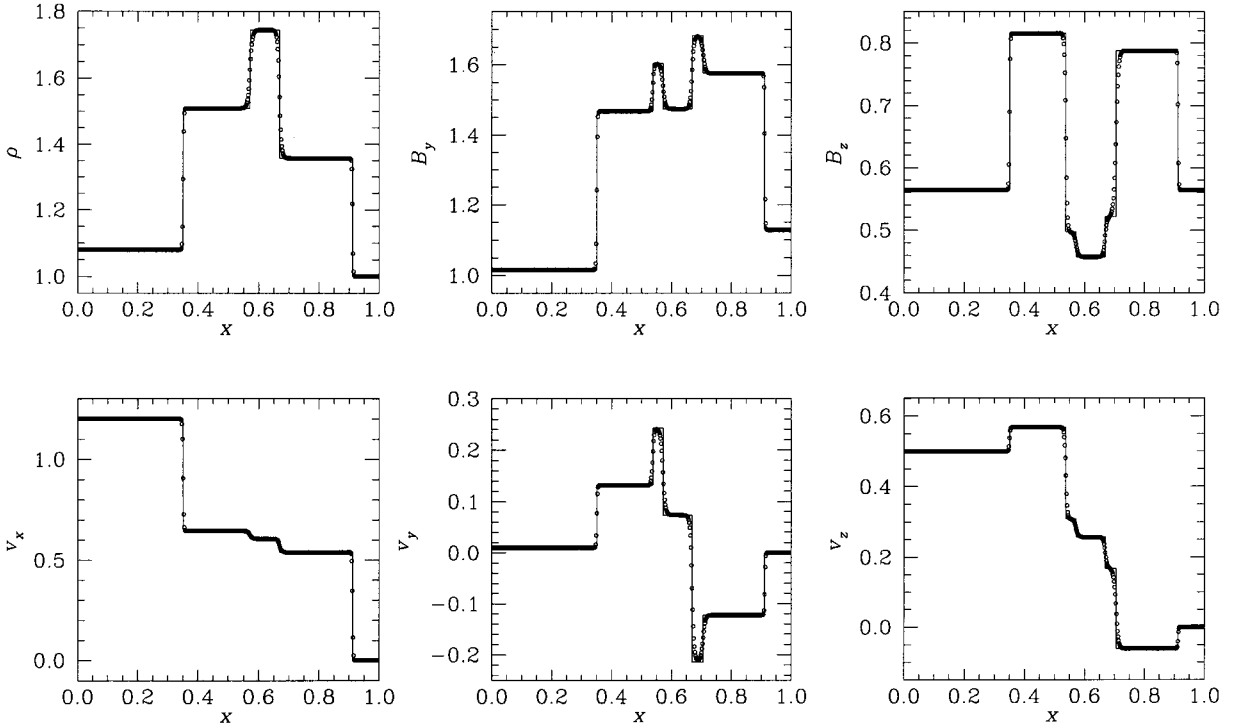
FIG. 1a

FIG. 1b

FIG. 1.—One-dimensional IMHD shock tube tests. (a) The initial condition is (ρ, v_x, v_y, v_z, B_y, B_z) = [1, 0, 0, 0, 5/($4\pi)^{1/2}$, 0] in the left region, (ρ, v_x, v_y, v_z, B_y, B_z) = [0.1, 0, 0, 0, 2/($4\pi)^{1/2}$, 0] in the right region, and $B_x = 3/(4\pi)^{1/2}$ and $a = 1$ for the whole computational interval. A snapshot at $t = 0.1$ shows from left to right (1) fast rarefaction, (2) slow rarefaction, (3) slow shock, and (4) fast shock. (b) The initial condition is (ρ, v_x, v_y, v_z, B_y, B_z) = [1.08, 1.2, 0.01, 0.5, 3.6/($4\pi)^{1/2}$, 2/($4\pi)^{1/2}$] in the left region, (ρ, v_x, v_y, v_z, B_y, B_z) = [1, 0, 0, 0, 4/($4\pi)^{1/2}$, 2/($4\pi)^{1/2}$] in the right region, and $B_x = 2/(4\pi)^{1/2}$ and $a = 1$ for the whole computational interval. A snapshot at $t = 0.2$ shows from left to right (1) fast shock, (2) rotational discontinuity, (3) slow shock, (4) slow shock, (5) rotational discontinuity, and (6) fast shock. (c) The initial condition is (ρ, v_x, v_y, v_z, B_y, B_z) = (0.12, 24, 0, 0, 3/$\sqrt{4\pi}$, 0) in the left region, (ρ, v_x, v_y, v_z, B_y, B_z) = [0.3, -15, 0, 0, 0, 3/($4\pi)^{1/2}$] in the right region, and $B_x = 0$ and $a = 1$ for the whole computational interval. A snapshot at $t = 0.2$ shows from left to right (1) magnetosonic shock, (2) tangential discontinuity, and (3) magnetosonic shock. (d) The initial condition is (ρ, v_x, v_y, v_z, B_y, B_z) = (1, -1, 0, 0, 1, 0) in the left region, (ρ, v_x, v_y, v_z, B_y, B_z) = (1, 1, 0, 0, 1, 0) in the right region, and $B_x = 0$ and $a = 1$ for the whole computational interval. A snapshot at $t = 0.16$ shows from left to right (1) magnetosonic rarefaction, and (2) magnetosonic rarefaction. Open circles represent the numerical solution, while lines represent the analytic solution with an exact nonlinear Riemann solver. The calculations have been done with 512 cells.
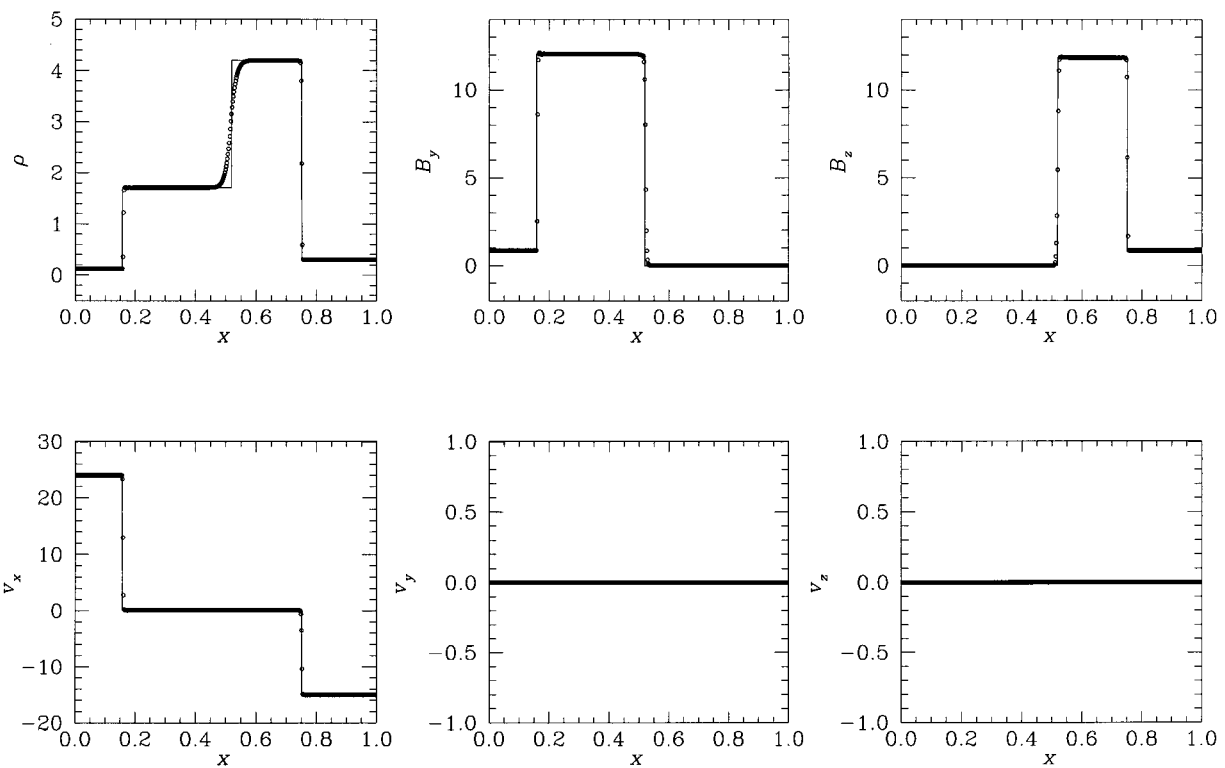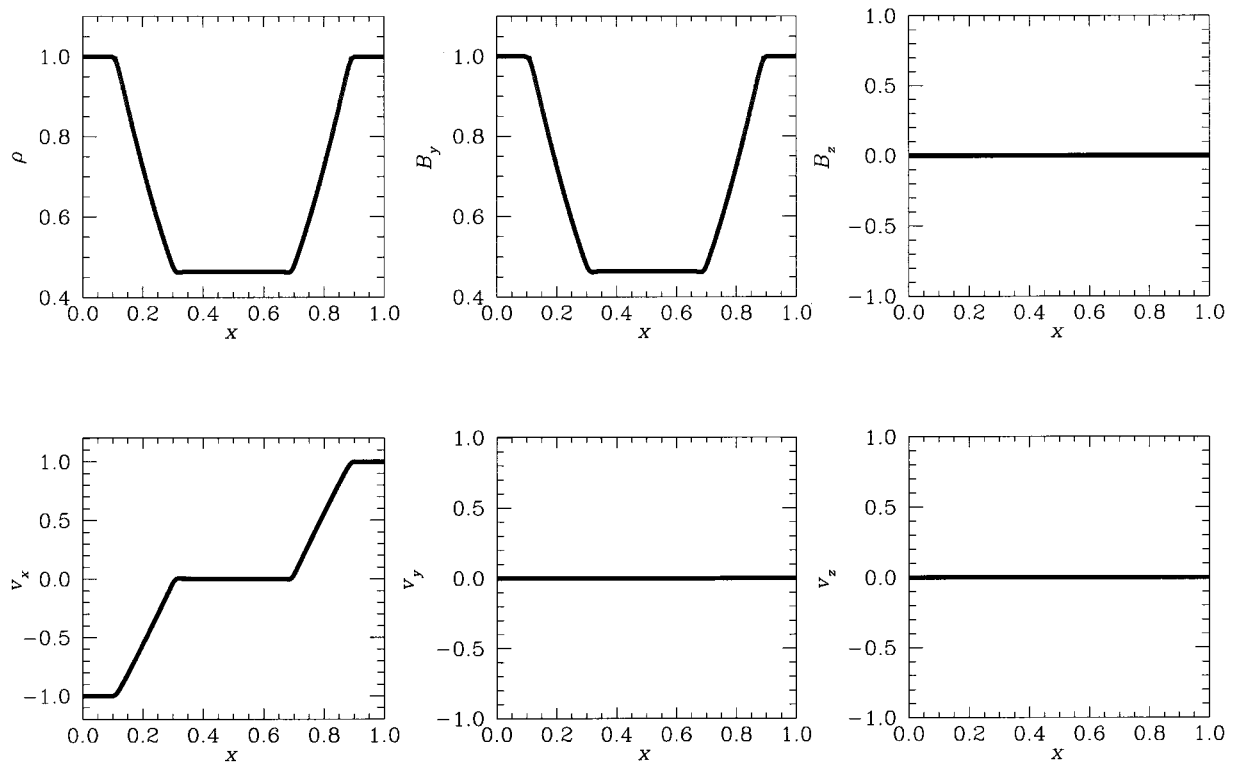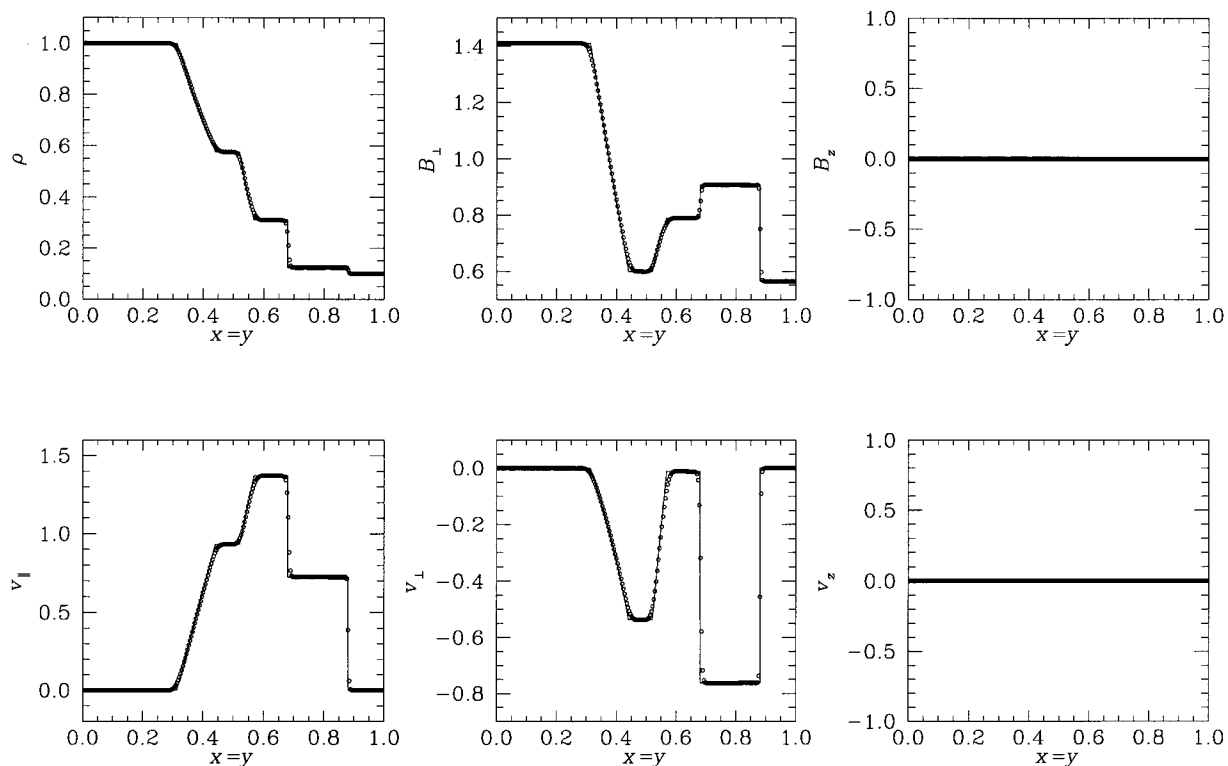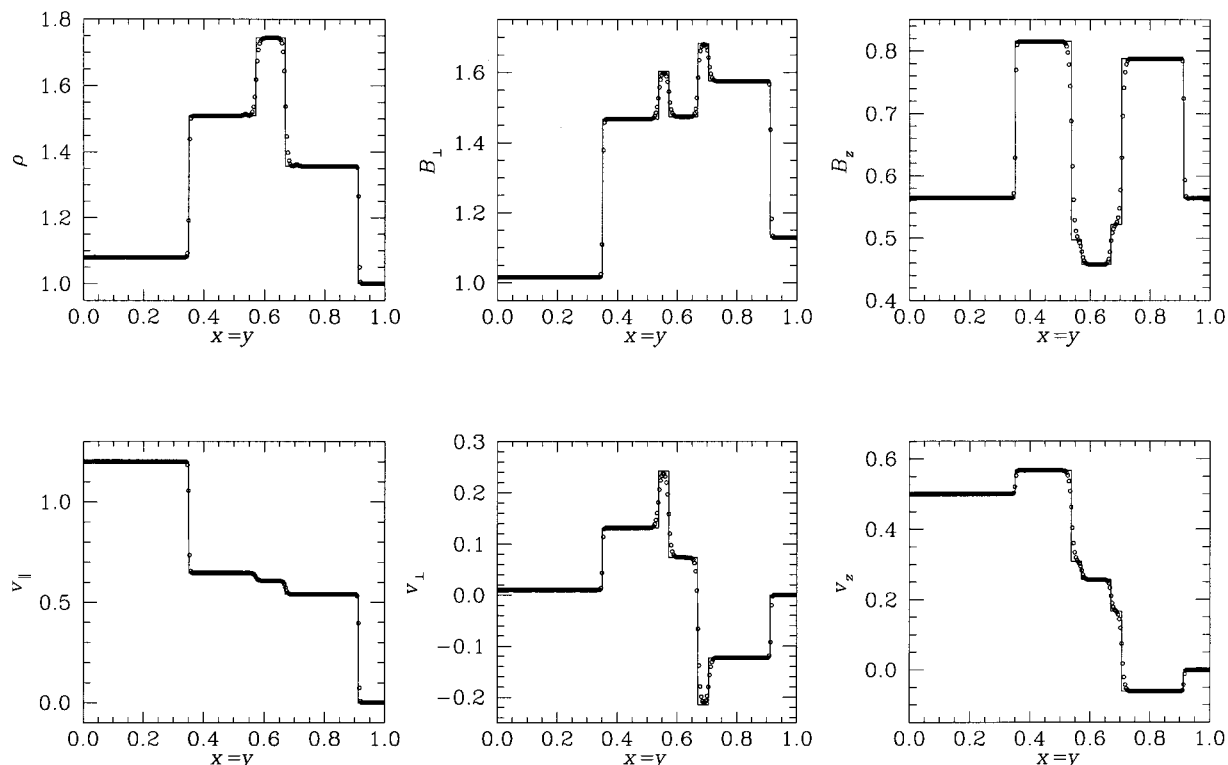
FIG. 1c

Fig. 1d

FIG. 2a

FIG. 2b

FIG. 2.— Two-dimensional IMHD shock tube tests. (a) The initial condition is $(\rho, v_\parallel, v_\perp, v_z, B_\perp, B_z) = [1, 0, 0, 0, 5/(4\pi)^{1/2}, 0]$ in the lower left region, $(\rho, v_\parallel, v_\perp, v_z, B_\perp, B_z) = [0.1, 0, 0, 0, 2/(4\pi)^{1/2}, 0]$ in the upper right region, and $B_\parallel = 3/(4\pi)^{1/2}$ and $a = 1$ in the whole computational domain. The structures shown at $t = 0.1\sqrt{2}$ along a diagonal line joining the two points (0, 0) to (1, 1) are same as those of Fig. 1a. (b) The initial condition is $(\rho, v_\parallel, v_\perp, v_z, B_\perp, B_z) = [1.08, 1.2, 0.01, 0.5, 3.6/(4\pi)^{1/2}, 2/(4\pi)^{1/2}]$ in the lower left region, $(\rho, v_\parallel, v_\perp, v_z, B_\perp, B_z) = [1, 0, 0, 0, 4/(4\pi)^{1/2}, 2/(4\pi)^{1/2}]$ in the upper right region, and $B_\parallel = 2/(4\pi)^{1/2}$ and $a = 1$ in the whole computational domain. The structures shown at $t = 0.2\sqrt{2}$ along a diagonal line joining the two points (0, 0) to (1, 1) are same as those of Fig. 1b. Open circles represent the numerical solution, while lines represent the analytic solution with an exact nonlinear Riemann solver. The calculations have been done with 256×256 cells.

515

(RJF). We define the decay rate as

$$\Gamma_A = \frac{1}{2}\left(\frac{\mu}{\rho_0} + \eta\right)k^2 \, . \tag{3.6}$$

For the decay test of a linear Alfvén wave with the IMHD code, we have set up an initial condition such that, $\rho_0 = 1$, $\delta v_z = v_{\mathrm{amp}} c_A \sin(k_x x + k_y y)$, $\boldsymbol{B} = 1 \cdot \hat{\boldsymbol{x}}$, and all other quantities are equal to zero. The calculations have been done in a square periodic box with size $L = 1$ using from 8×8 cells to 128×128 cells by increasing twice the number of cells in each direction. We set $k_x = k_y = 2\pi/L$. Numerical parameters used are $\epsilon_k = 0$ and $C_{\mathrm{cour}} = 0.9$ (the result is not sensitive to these values). Figure 3a shows the decay of the Alfvén wave calculated with 32×32 cells. By fitting the peak points of the decay pattern with respect to time, we have estimated decay rate. In Figure 3b the resulting normalized decay rates as well as
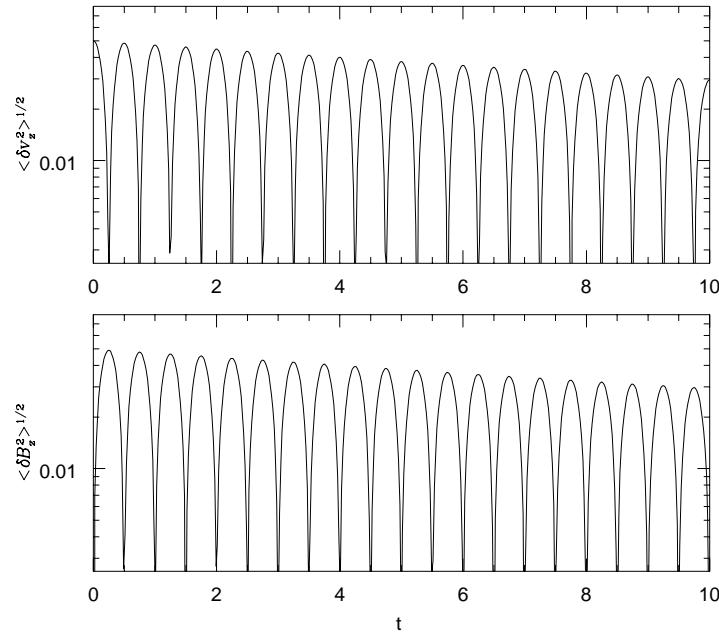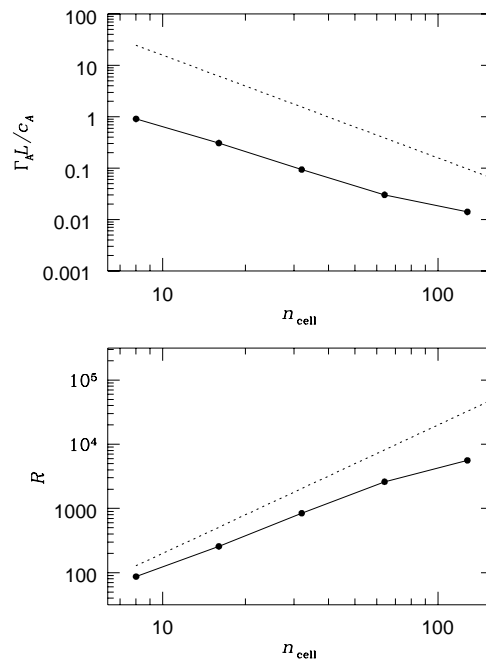

FIG. 3a

FIG. 3b

FIG. 3.—(a) Time evolution of $\langle \delta B_z^2 \rangle^{1/2}$ and $\langle \delta v_z^2 \rangle^{1/2}$ in the decay test of a two-dimensional Alfvén wave. Initially a standing Alfvén wave has been set up in a computational domain with 32×32 cells, and its oscillation has been followed. (b) Normalized decay rate $\Gamma_A L/C_A$, and magnetic Reynolds number, R, as a function of cells along one direction of the computation domain. At a given resolution, the peak-to-peak decay rate of the rms of z-velocity (top) and the corresponding Reynolds number (bottom) are plotted with filled circles, respectively. The calculations have been done with 8×8, 16×16, 32×32, 64×64, and 128×128 cells. For comparison, dotted lines of $(\Gamma_A L/c_A) \propto n_{\mathrm{cell}}^{-2}$ and $R \propto n_{\mathrm{cell}}^2$ are drawn.

Reynolds numbers (see RJF for definition) are shown. Numerical Reynolds numbers scale almost as $R \propto n_{\rm cell}^2$, indicating that the code has a second-order accuracy. Compared to the adiabatic MHD code, the IMHD code has smaller (up to 50%) numerical dissipation. This is partly because the IMHD code has one less mode (entropy mode).

3.3. *Parker Instability under a Uniform Gravity*

Nonlinear development of the Parker instability under a point-mass–dominated gravity was simulated by Matsumoto and his collaborators (Matsumoto et al. 1988; Matsumoto et al. 1990; Matsumoto & Shibata 1992). And recently, Basu, Mouschovias, & Paleologou (1996, 1997) simulated the nonlinear evolution of the Parker instability under a uniform gravity. As the final test of our IMHD code, we have also followed the nonlinear evolution of the Parker instability under the uniform gravity. By comparing our results with those in Basu et al. (1996), the code's ability to handle a practical problem of astrophysics can be proved.

Since the Parker system is assumed initially to be in an isothermal equilibrium, an IMHD code is a natural tool for simulations. In the IMHD equations, the externally given gravity $g\hat{z}$ is treated as a source term and placed on the right hand-side of equation (2.5) with the source vector defined by $S = (0, 0, 0, -gv_z, 0, 0, 0)^T$. The gravity has the z-component only, so the source term is evaluated only when the state vector is updated along the z-axis

$$\frac{\partial q}{\partial t} + \frac{\partial F_z}{\partial z} = S \, . \tag{3.7}$$

Since we use the Strang-type directional splitting in order to reduce multidimensional problems to one-dimensional ones, we also use the same technique to split the hyperbolic system with a source term into two parts, part A,

$$\frac{\partial q}{\partial t} + \frac{\partial F_z}{\partial z} = 0 \, , \tag{3.8}$$

and part B,

$$\frac{\partial q}{\partial t} = S \, . \tag{3.9}$$

Part A is solved by the TVD algorithm, and part B by a forward time difference. To minimize a "splitting error," part A and part B are solved by a BAB sequence with time step size $0.5\Delta t$ for part B and Δt for part A. The step size Δt is determined from the Courant condition.

The Parker system composed of isothermal gas and magnetic field $\hat{y}B_0(z)$ takes under the uniform gravity an equilibrium configuration given by

$$\frac{\rho_0(z)}{\rho_0(0)} = \frac{B_0^2(z)}{B_0^2(0)} = \exp\left(-z/H\right) \, , \tag{3.10}$$

where the gas scale height is $H \equiv (1 + \alpha)a^2/g$ and the initial ratio of the magnetic to the gas pressure $\alpha (\equiv B_0^2/[2\rho_0 a^2])$ is assumed a constant. We have chosen $\alpha = 1.0$ in the simulation.

The computation domain covers $0 \le y \le 12H$ and $0 \le z \le 12H$. According to the linear stability analysis $12H$ is the horizontal wavelength corresponding to the maximum growth rate (Parker 1966). Periodic condition has been used in the y-boundaries, while reflecting condition in the z-boundaries. The density scale height H, the isothermal sound speed a, the initial midplane density $\rho_0(0)$, and the initial midplane field strength $B_0(0)$ have been chosen as the units of length, velocity, density, and magnetic field, respectively.

To initiate the instability we have added random velocity perturbations to the equilibrium profile of equation (3.10). Standard deviation of the perturbation velocity is $10^{-4}a$ for each of the velocity components. To check whether the system follows, in the initial stage, the prescription of the linear analysis, we plot the logarithmic values of the rms velocity against time. In Figure 4a the dotted and dashed lines are for the horizontal and vertical components of the velocity, respectively. In the same figure the solid line represents the linear growth of a rate 0.34, which is the maximum growth rate of the system. At the very early stage the system undergoes a transient phase of adjustment and then quickly develops the Parker instability at the rate predicted by the linear analysis. The linear growth gets saturated near $t \simeq 40$.

The whole development of the Parker instability may be divided into three phases: The linear phase lasts up to $t \simeq 40$, from then on the system undergoes the nonlinear phase until $t \simeq 57$, and finally it reaches the damping oscillatory phase. Iso-contours and gray maps for density (*left*) and magnetic field lines and velocity vectors (*right*), in Figure 4b, present snapshots of the system at the end of the linear phase ($t = 40$), at the end of the nonlinear phase ($t = 57$), and finally at $t = 80$ of the damping oscillatory phase.

In the linear phase the perturbations grow predominantly in the upper region. In the nonlinear phase the perturbations gradually move toward the midplane. Through the linear and nonlinear phases, our simulation renders features that closely agree with those of Basu et al. (1996). As more matter accumulates, already compressed gas in the valley gets over-compressed. The increased gas pressure bounces the valley matter back to the upper region, and at the same time the built-up pressure at the valley gets somewhat eased off. This in turn brings the matter back to the valley. The system now enters the oscillatory phase of the Parker instability. As the field lines are pushed deep down to the valley by the weight of overlying matter, the curvature of the lines becomes small to the degree that magnetic field lines undergo reconnection. Owing to the reconnection the matter drops down off the reconnected line, thereby the matter is allowed to move across the magnetic field line. The field
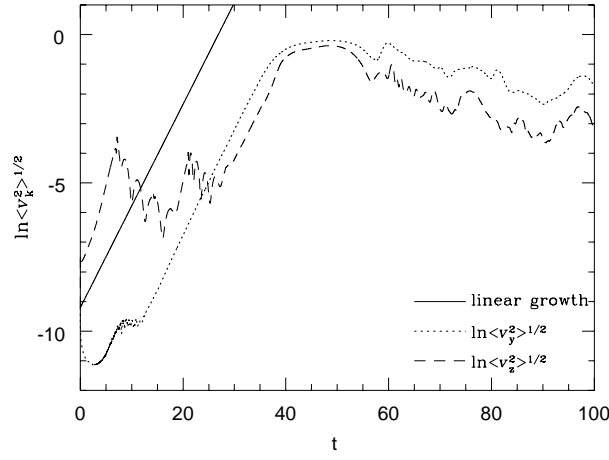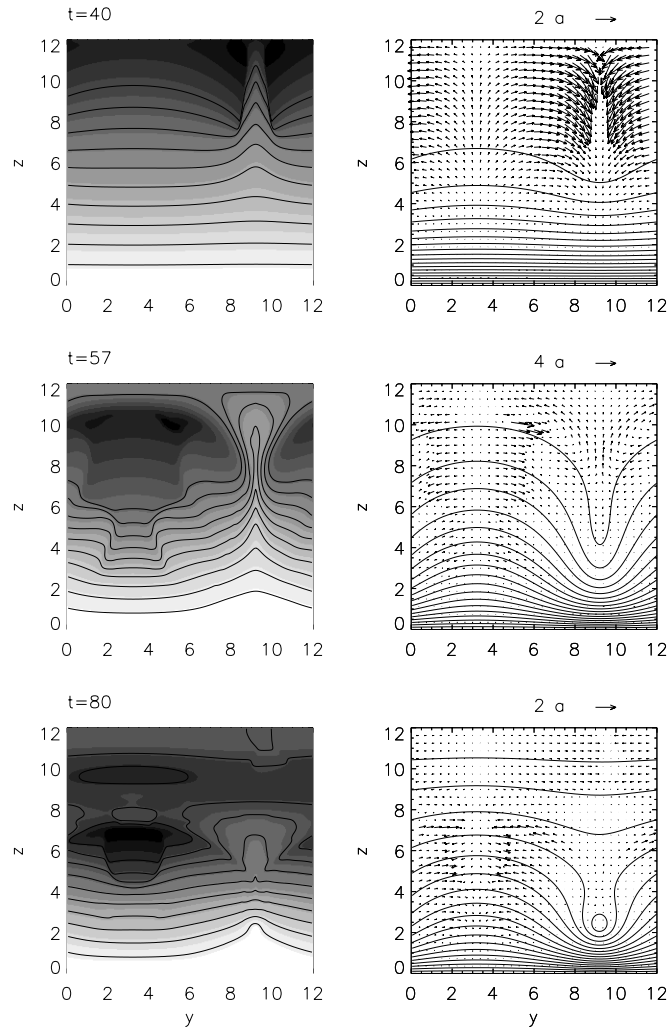
FIG. 4a

FIG. 4b

FIG. 4.—(a) Time evolution of the rms of the horizontal velocity, $\langle v_y^2 \rangle^{1/2}$, and the vertical velocity, $\langle v_z^2 \rangle^{1/2}$, in a simulation of the Parker instability under a uniform gravity. The magnetohydrostatic equilibrium state together with random velocity perturbations has been given as an initial condition of the simulation in the computational domain of 256×256 cells. The solid line represents the predicted maximum linear growth with perturbation wavelength $\lambda_y = 12$, and $\lambda_z/2 = 12$. The normalization units are the isothermal sound speed and the scale height. (b) Evolution of the Parker instability under a uniform gravity. At three time epochs $t = 40$ (top), $t = 57$ (middle), and $t = 80$ (bottom), gray maps of density together with equidensity lines are plotted in the left panels, and the velocity vectors with magnetic field lines in the right panels. The values of the 10 equidensity lines are the initial exponential densities at $z = 1, \ldots, 10$. Magnetic field lines are chosen so that the magnetic flux between two consecutive lines is constant. At each time epoch, the unit of the velocity vectors is represented.

line is now relieved from the burden of supporting the gas against the external gravity and floats upward. On the other hand, the field line located just below the reconnected one has to support more weight than before. Consequently this line now gets reconnected. In this way a redistribution of matter with respect to the field lines continues to occur until there is no more reconnection. The system finally settles in an equilibrium. Since the reconnection drives the system to violate the flux-freezing condition, the final configuration of the system is different from that of the Mouschovias (1974) equilibrium.

4. CONCLUSIONS

We have developed one-dimensional and multi-dimensional numerical codes to solve the IMHD equations, which are isothermal analogues of the previous adiabatic codes (RJ; RJF). Both the isothermal and adiabatic codes are based on the same scheme, an explicit finite-difference scheme on an Eulerian grid called TVD, which is a second-order–accurate extension of the Roe-type upwind scheme. The shock tube tests have shown that both codes capture correctly all the structures in MHDs. From the decay test of a linear Alfvén wave, we have found that numerical dissipation of the IMHD code is somewhat smaller than that of the adiabatic MHD code.

The robustness of the adiabatic code has been demonstrated through the simulations of MHD flows such as the Kelvin-Helmholtz instability (Frank et al. 1996; Jones et al. 1997) and jets (Frank et al. 1998; Jones, Ryu, & Engel 1999), and that of the isothermal code has been done through the simulation of the Parker instability under the uniform gravity in this paper. Furthermore, both codes are fast enough to simulate multidimensional, astrophysical MHD flows using modest computational resources. Both codes run at about 400 MFlops on a Cray C90 processor (RJF), and the isothermal code updates zones about twice as fast as the adiabatic code. Together with the adiabatic code, the isothermal code is a useful tool to study the nonlinear evolution of astrophysical MHD flows.

REFERENCES

Balsara, D. S., 1998a, ApJS, 116, 119
———. 1998b, ApJS, 116, 133
Basu, S., Mouschovias, T. Ch., & Paleologou, E. V. 1996, Astron. Lett., 34, 333
———. 1997, ApJ, 480, L55
Brackbill, J. U., & Barnes, D. C. 1980, J. Comput. Phys., 35, 426
Brio, M., & Wu, C. C. 1988, J. Comput. Phys., 75, 400
Colella, P., & Woodward, P. R. 1984, J. Comput. Phys., 54, 174
Dai, W., & Woodward, P. R. 1994a, J. Comput. Phys., 111, 354
———. 1994b, J. Comput. Phys., 115, 485
Draine, B. T., & McKee, C. F. 1993, AR&A, 31, 373
Evans, C. R., & Hawley, J. F. 1988, ApJ, 332, 659
Frank, A., Jones, T. W., Ryu, D., & Gaalaas, J. B. 1996, ApJ, 460, 777
Frank, A., Ryu, D., Jones, T. W., & Noriega-Crespo, A. 1998, ApJ, 494, L79
Godunov, S. K. 1959, Math. Sbornik., 47, 271
Harten, A. 1983, J. Comput. Phys., 49, 357
Harten, A., Engquist, B., Osher, S., Chakravarthy, S. R. 1987, J. Comput. Phys., 71, 231
Jeffrey, A., & Taniuti, T. 1964, Nonlinear Waves Propagation (New York: Academic)
Jones, T. W., Gaalaas, J. B., Ryu, D., & Frank, A. 1997, ApJ, 482, 230
Jones, T. W., Ryu, D., & Engel, A. 1999, ApJ, in press
LeVeque, R. J. 1997, in 27th Saas-Feé Advanced Course Lecture Notes, Computational Methods in Astrophysical Fluid Flows, ed. O. Steiner & A. Gautschy (Berlin: Springer)

Matsumoto, R., Horiuchi, T., Hanawa, T., & Shibata, K. 1990, ApJ, 356, 259
Matsumoto, R., Horiuchi, T., Shibata, K., & Hanawa, T. 1988, PASJ, 40, 171
Matsumoto, R., & Shibata, K. 1992, PASJ, 44, 167
Mouschovias, T. Ch. 1974, ApJ, 192, 37
Parker, E. N. 1966, ApJ, 145, 811
Powell, K. G., Roe, P. L., Myong, R. S., Combosi, T., & De Zeeuw, D. 1995, in Numerical Methods for Fluid Dynamics, ed. K. W. Morton & M. J. Baines (Oxford: Clarendon), 163
Roe, P. L. 1981, J. Comput. Phys., 43, 357
Roe, P. L., & Balsara, D. S. 1996, SIAM J. Appl. Math., 56, 57
Ryu, D., & Jones, T. W. 1995, ApJ, 442, 228 (RJ)
Ryu, D., Jones, T. W., & Frank, A. 1995, ApJ, 452, 785 (RJF)
Ryu, D., Miniati, F., Jones, T. W., & Frank, A. 1998, ApJ, 509, 244
Strang, G. 1968, SIAM J. Numer. Anal., 5, 506
Truelove, J. K., Klein, R. I., McKee, C. F., Holliman, J. H., II, Howell, L. H., Greenough, J. A., & Woods, D. T. 1988, ApJ, 495, 821
Van Leer, B. 1979, J. Comput. Phys., 32, 101
Zachary, A. L., & Colella, P. 1992, J. of Comput. Phys., 99, 341
Zachary, A. L., Malagoli, A., & Colella, P. 1994, SIAM J. Sci. Comput., 15, 263